

On-Chip Hybrid Photonic–Plasmonic Light Concentrator for Nanofocusing in an Integrated Silicon Photonics Platform

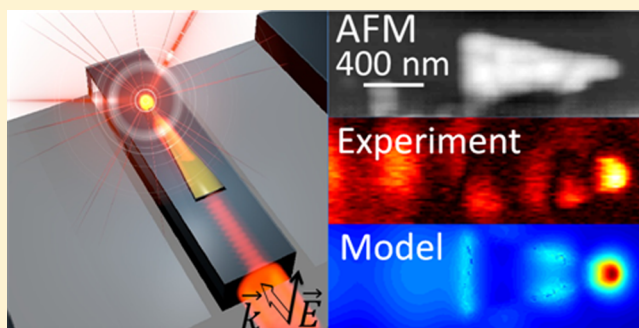
Ye Luo,^{†,||} Maysamreza Chamanzar,^{†,⊥} Aniello Apuzzo,[‡] Rafael Salas-Montiel,[‡] Kim Ngoc Nguyen,[‡] Sylvain Blaize,^{*,‡,||} and Ali Adibi^{*,†,§}

[†]School of Electrical and Computer Engineering, Georgia Institute of Technology, Atlanta, Georgia 30332, United States

[‡]Laboratoire de Nanotechnologie et d'Instrumentation Optique, CNRS-UMR 6281, Université de technologie de Troyes, Troyes 10010, France

S Supporting Information

ABSTRACT: The enhancement and confinement of electromagnetic radiation to nanometer scale have improved the performances and decreased the dimensions of optical sources and detectors for several applications including spectroscopy, medical applications, and quantum information. Realization of on-chip nanofocusing devices compatible with silicon photonics platform adds a key functionality and provides opportunities for sensing, trapping, on-chip signal processing, and communications. Here, we discuss the design, fabrication, and experimental demonstration of light nanofocusing in a hybrid plasmonic–photonic nanotaper structure. We discuss the physical mechanisms behind the operation of this device, the coupling mechanisms, and how to engineer the energy transfer from a propagating guided mode to a trapped plasmonic mode at the apex of the plasmonic nanotaper with minimal radiation loss. Optical near-field measurements and Fourier modal analysis carried out using a near-field scanning optical microscope (NSOM) show a tight nanofocusing of light in this structure to an extremely small spot of $0.00563(\lambda/(2n(r_{\max})))^3$ confined in 3D and an exquisite power input conversion of 92%. Our experiments also verify the mode selectivity of the device (low transmission of a TM-like input mode and high transmission of a TE-like input mode). A large field concentration factor (FCF) of about 4.9 is estimated from our NSOM measurement with a radius of curvature of about 20 nm at the apex of the nanotaper. The agreement between our theory and experimental results reveals helpful insights about the operation mechanism of the device, the interplay of the modes, and the gradual power transfer to the nanotaper apex.



KEYWORDS: Plasmonics, near-field scanning optical microscopy, silicon photonics, integrated optics, nanofocusing

Focusing of lightwaves beyond the diffraction limit in plasmonic structures has opened up new opportunities for applications involving light–matter interaction such as optical trapping/tweezing^{1–3} and local heat generation.⁴ On the other hand, strong enhancement of the optical field in plasmonic structures enables a plethora of applications in sensing,^{5,6} nonlinear optics,⁷ and single nanoemitters.⁸ To tightly focus lightwave to a nanometer-scale spot and to avoid electromagnetic field radiation into the free-space, different structures that gradually decrease in size have been theoretically proposed such as sharp metallic tips,^{9,10} metallic wedges,^{11,12} dielectric wedges,¹³ conical structures,^{14,15} sharp metallic V-grooves,¹⁶ nanotapered metallic waveguides,^{17,18} and stripes.¹⁹ Experimental demonstrations of radiation nanofocusing were done in nanotapered metallic grooves,^{20,21} plasmonic dimple lenses,²² metallic pyramids,²³ and metal–insulator–metal three-dimensional linear nanotapers.²⁴ All these impressive demonstrations were carried out through illuminating the structure with free-space radiative modes. For many practical applications, it is desired to have light nanofocusing capability on a chip in an

integrated platform for the efficient illumination and detection of light and for integration with a number of other photonic functionalities. Recently, the integration of surface plasmon nanofocusing structures onto silicon (Si) photonic waveguides was proposed²⁵ and demonstrated.^{26–28} Indeed, Si photonics is a well-established platform that has a great potential for the integration of several photonic and plasmonic functionalities into a single-chip.^{29–33}

We previously proposed and theoretically studied a plasmonic light concentrator (PLC) integrated on silicon nitride (Si_3N_4) optical waveguides for visible and near-infrared light nanofocusing.²⁸ In this Letter, we report the design, implementation, and demonstration of efficient light nanofocusing in a PLC vertically integrated on a Si waveguide. The vertical integration of the plasmonic light concentrator with the

Received: September 9, 2014

Revised: December 23, 2014

Published: January 6, 2015

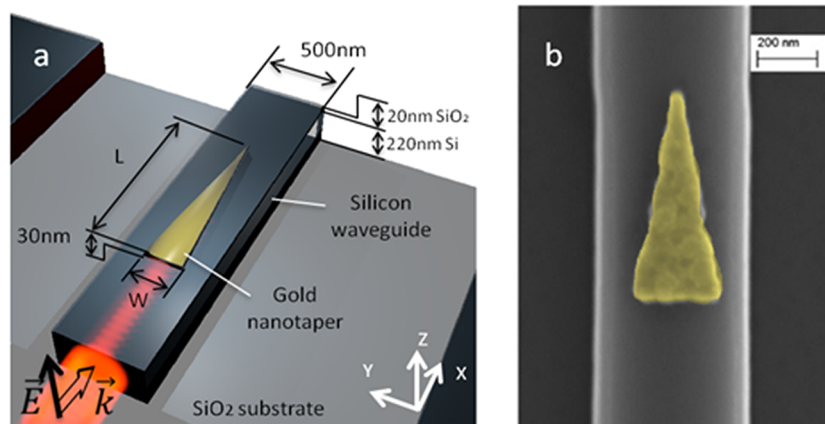


Figure 1. (a) Schematic illustration of the hybrid nanotapered PLC integrated on silicon ridge waveguide. The hybrid PLC consists of a gold isosceles triangle of 300 nm base width and 750 nm length placed on top of a 500 nm by 220 nm Si waveguide with a 20 nm thick SiO₂ buffer layer. The PLC tip has radius of curvature of 20–30 nm. The fundamental TM-like mode of the Si waveguide is gradually coupled to the plasmonic modes of the PLC, which will be focused at the tip of the triangular nanotaper. (b) Scanning electron micrograph (SEM) of a fabricated structure.

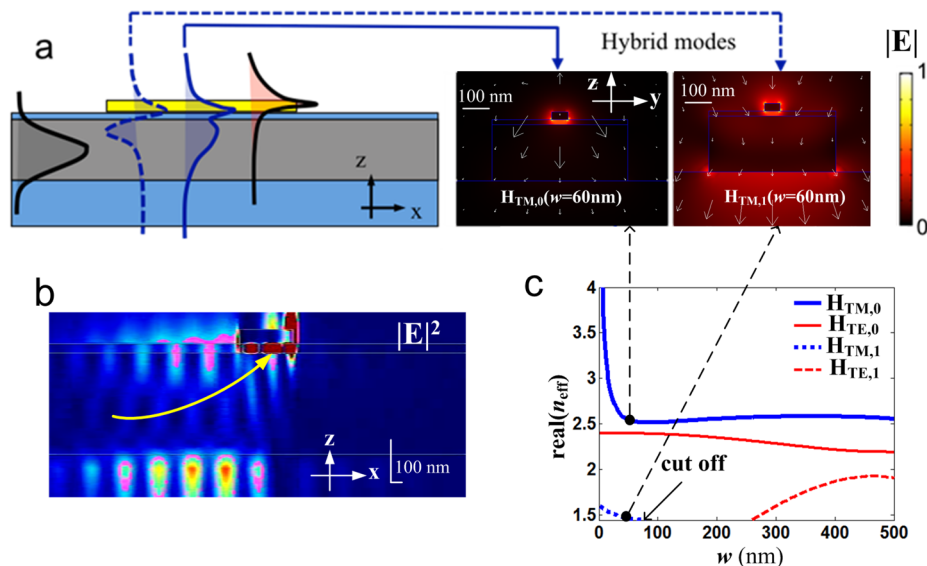


Figure 2. (a) Principle of operation of the PLC integrated on a Si waveguide. Directional photonic–plasmonic coupler in the plane x – z at $y = 0$. The normalized electric field profiles for the asymmetric $H_{TM,0}$ and the symmetric $H_{TM,1}$ modes in the transversal plane y – z for $w = 60$ nm calculated at $\lambda = 1550$ nm. (b) Snapshot of a time-domain light propagation video (available in the Supporting Information) using in the longitudinal plane x – z at $y = 0$. The length of the triangle taper is 750 nm. Light propagates from left to right. The yellow arrow is a guide for the eye visualizing the energy transfer from the dielectric waveguide into the apex of the nanotaper. (c) Modal analysis of the vertical plasmonic–photonic coupler. Mode effective indices of the TM-like ($H_{TM,0}$ and $H_{TM,1}$) and TE-like ($H_{TE,0}$ and $H_{TE,1}$) modes (blue and red curves, respectively), as a function of the width w of the corresponding gold strip.

photonic waveguiding structure is compatible with the dense integration of different photonic and plasmonic functionalities on the same chip. In contrast to some other previously proposed structures where the plasmonic light concentrator is integrated in-line with photonic waveguides,²⁷ our two-layer (photonic and plasmonic) implementation is a unique and modular design commensurate with the requirements for a scalable process.³⁴ Such a configuration provides strong and low-loss nanofocusing of near-infrared electromagnetic radiation over a broad bandwidth and can address the integration challenges of existing implementations.³⁵ We discuss the design, fabrication and optical characterizations of the hybrid PLC structure. To characterize the performance of the hybrid photonic–plasmonic device for the focusing of light at nanoscale, we used a near-field scanning optical microscope

(NSOM) to directly measure the PLC performance. Indeed, NSOM is a powerful tool that not only can reveal the physical mechanisms at the nanometer scale³⁶ but also can be used for mode analysis on optical waveguides. Although most of the NSOM demonstrations of nanofocusing in literature are limited only to the local plasmonic regions, we will present in this paper both characterizations on our device: (1) measurement of the near-field pattern around plasmonic nanotaper of the PLC, and (2) experimental mode analysis of the photonic modes in the regions of the bare waveguide before and after the plasmonic nanotaper region. In particular, using the latter characterizing approach, we are able to provide quantitative data for analyzing mode losses, transmission and reflection power coefficients on our nanofocusing structure. Such an analysis can only be done with the vertical coupling scheme in

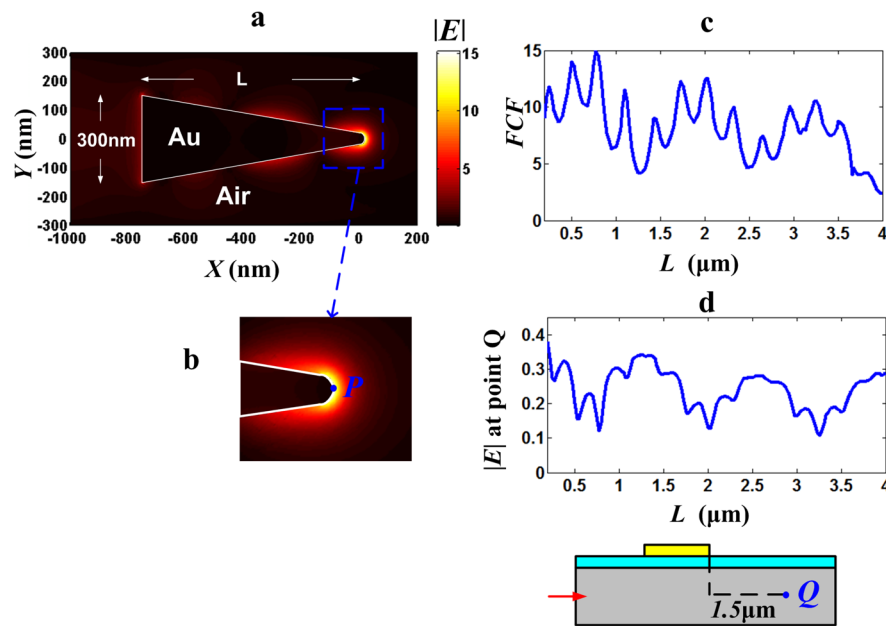


Figure 3. (a) Electric field distribution in a plane at the middle of the gold layer with (b) a zoom at its apex. The field is normalized to the average electric field amplitude in the corresponding bare waveguide. The field concentration factor (FCF) is the normalized field amplitude at the apex point “P”. (c) The field concentration factor (FCF) when the curvature radius of the tip is 20 nm and (d) the electric field amplitude at point “Q” versus the length L of the nanotaper, also normalized to the average electric field amplitude in the corresponding bare waveguide.

our device that separates the plasmonic hotspot from the underlying optical waveguide.

Our numerical simulations of the PLC and the agreement with the experimental results provide helpful insights about the operation mechanism and performances as well as the strategies for the design of efficient nanofocusing structures.

The hybrid photonic–plasmonic light concentrator presented here consists of a gold (Au) triangular nanotaper that is integrated on a Si ridge waveguide in a silicon-on-insulator (SOI) substrate (Figure 1a). In this structure, a thin (with a thickness of ~ 20 nm) silicon dioxide (SiO_2) layer separates the gold nanotaper (with a thickness of ~ 30 nm) from the Si waveguide and acts as a buffer layer to control the coupling between the photonic and the plasmonic modes.

The length L of the nanotaper is designed in a range of 400–1500 nm and the width at its base is 300 nm. The dimensions of the Si waveguide are 500 nm by 220 nm. The hybrid device was fabricated using two steps of electron beam lithography based on the optimized process explained in detail in our previous work.³⁴ The scanning electron micrograph (SEM) of a hybrid PLC device realized in Si platform is shown in Figure 1b. Different sizes and shapes of the hybrid PLC device can be realized using the optimized fabrication method. Further details of the fabrication method are described in the Supporting Information.

The principle of operation of the integrated PLC can be understood using a numerical analysis to account for the strong coupling of different modes in the structure. The propagating photonic-guided mode in the Si waveguide with TM-like polarization (with the principal transverse component of the magnetic field along the width of the waveguide) excites hybrid plasmonic–photonic modes at the base of the triangle nanotaper. In the overlapping area, the Si waveguide and the metallic triangle form a superstructure. The electromagnetic energy is exchanged between the plasmonic and the photonic modes (Figure 2a). Because the width of the plasmonic

nanotaper is gradually decreased, the hybrid modes will conform to a predominant plasmonic mode that will eventually become localized at the tip of the triangle (Figure 2b).

Using an analogous analysis in our previous work,²⁸ the effective indices and the electromagnetic field profiles of the supported modes can be computed for the corresponding hybrid waveguide at each cross section along the hybrid structure, where the width w of the plasmonic nanotaper decreases. At each cross section, the hybrid waveguide is simulated using the finite element method (FEM) in COMSOL software to obtain the hybrid modes.

Two hybrid TM-like modes ($H_{\text{TM},0}$ and $H_{\text{TM},1}$) and two hybrid TE-like modes ($H_{\text{TE},0}$ and $H_{\text{TE},1}$) are supported by the hybrid structure at 1550 nm (Figure 2c). The TM-like modes have the principal component of the transverse magnetic field along the width of the waveguide and one component of the dominant transverse electric field normal to the top surface of the waveguide. As we will discuss later, these TM-like modes are the modes of interest and can result in the nanofocusing of light at the tip of the triangle as opposed to the TE-like modes, which have the principal component of the transverse electric field along the width of the waveguide. The $H_{\text{TM},0}$ and $H_{\text{TE},0}$ modes are guided modes whereas the $H_{\text{TM},1}$ and $H_{\text{TE},1}$ modes are leaky modes for a width w between 80 and 260 nm. However, as it can be seen from Figure 2c, the $H_{\text{TM},1}$ mode becomes guided for a gold width less than 80 nm.

For the incident fundamental TM-like photonic mode of the Si waveguide at wavelength 1550 nm, only the $H_{\text{TM},0}$ and $H_{\text{TM},1}$ hybrid modes can be excited at the input of the plasmonic nanotaper (i.e., at $w = 300$ nm). As soon as these supermodes are excited, they propagate through the plasmonic nanotaper and they couple through a directional coupling mechanism. The beat length, defined as the length over which the relative phase of the supermodes differ by 2π , is denoted by BL and is inversely proportional to the real part of the difference between their effective indices and can be obtained as

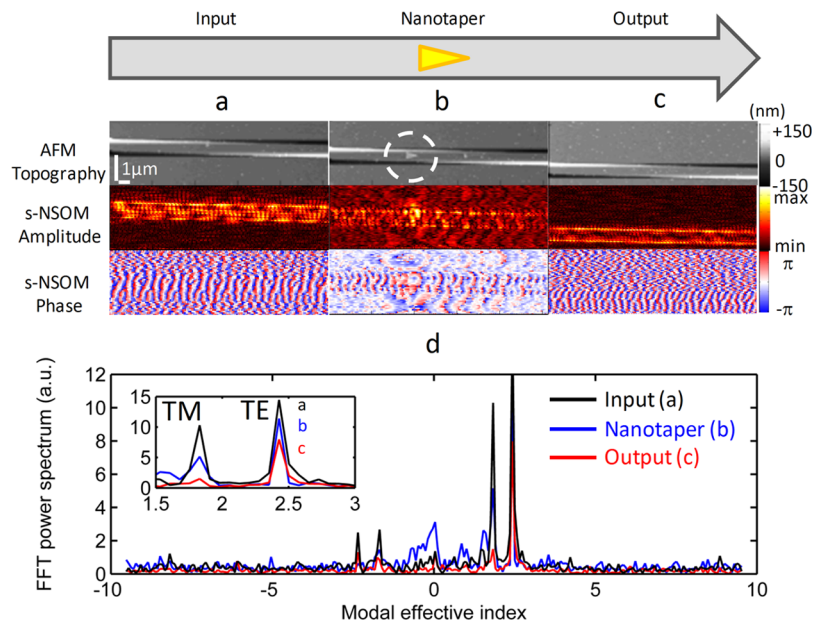


Figure 4. Measured optical near field along the integrated PLC under a light excitation at 1550 nm with an uncontrolled polarization. The upper panel represents the integrated PLC on a Si waveguide. (a) AFM topography of the Si waveguide in the input zone before the plasmonic nanotaper. Optical amplitude and phase NSOM images showing the multimodal behavior of the waveguide. (b) AFM topography around the plasmonic triangle (inside the white circle). 2D NSOM mapping of the hybrid coupler reveals a strong interaction between the triangle nanotaper and the Si waveguide (c) AFM topography of the bare waveguide taken immediately after the coupling zone. The light pattern is a clear manifestation of a TE-like propagating mode. (d) FFT spectra of the complex electric field profile as a function of the modal effective index. Black, blue, and red curves are referred to the three different zones, where the NSOM measurement was performed: on the input zone of the waveguide, on the hybrid structure region, and on the output part of the waveguide. The inset shows only the forward propagating modes, where it can be seen that the TM-like and TE-like modes are consumed differently in three parts of the sample.

$BL(w) = \lambda / \text{real}(\Delta n_{\text{eff}}(w))$, where λ is the operation wavelength. BL decreases as the light propagates along the triangle because the effective index of $H_{\text{TM},0}$ increases as the width of the triangle nanotaper decreases. Finally, the effective index of $H_{\text{TM},0}$ increases asymptotically to infinity and thus the BL approaches zero at the apex of the triangle nanotaper, where the group velocity asymptotically approaches to zero. As a result, the electromagnetic energy is focused at the apex of the nanotaper in a very small volume. It is interesting to remark the unusually high effective index of the $H_{\text{TM},0}$ mode that tends to infinity (Figure 2c). As used in adiabatic theory based on Wentzel–Kramers–Brillouin (WKB) approximation,¹⁵ an eikonal parameter (also called adiabatic parameter) can be defined as $\delta = |(dw/dx)((d(k_0 n_{\text{eff}})^{-1})/dx)|$ in our setting. The eikonal parameter for the $H_{\text{TM},0}$ mode (the main adiabatically changing mode when width w is tapered down) is less than $0.5(dw/dx)$ when $w \geq 20$ nm. Such a light localization process is common to most geometry-induced plasmonics nanofocusing techniques,^{11,15} and is one of the main mechanisms to provide extreme light concentration in our proposed structure. On the other hand, another key mechanism for the light localization in our structure is the optimal energy transfer from the dielectric waveguide mode to the plasmonic taper. In our designed structure, a small averaged value of BL ($BL \sim 1.4 \mu\text{m}$) results in a transfer of energy over a short length of the taper. It should be noted, however, that the length of the taper should be carefully chosen so that the transferred energy is maximum at the taper apex.²⁸

Although the modal analysis of the hybrid nanotaper nanofocusing structure at different cross sections provides an understanding of the interplay of different modes in the formation of a high intensity region at the apex of the

plasmonic nanotaper, a numerical study of the propagation of light through the structure was conducted with the 3D finite-difference time-domain (FDTD) method using a commercial-grade simulator from “Lumerical Solutions”. We simulated the structure using the FDTD with a TM-like mode input as a time-domain Gaussian pulse of 30 fs. A snapshot of the time domain light propagation video (full video available in the Supporting Information) on the intensity of electrical field in the longitudinal x – z plane at $y = 0$ for a time-domain propagation along the hybrid structure is shown in Figure 2b. The length L of the triangle taper in the simulation is 750 nm. The FDTD simulations confirm the modal analysis predictions that the electromagnetic energy can be transferred from the core of the waveguide to the plasmonics nanotaper and be strongly confined by the PLC at the apex of the triangular nanotaper as evidenced in Figure 3a, where the normalized electric field profile around the nanotaper on x – y plane is plotted. The zoomed-in version of the field profile near the nanotaper is shown in Figure 3b.

As in our theoretical paper,²⁸ to estimate the strength of the electric field concentration, we introduced a field concentration factor (FCF) defined as the electric field amplitude at the apex of the nanotaper (point “P” in Figure 3b) normalized to the average electric field amplitude in the core region of a corresponding bare waveguide. This figure of merit for the PLC depends on the coupling efficiency, the material and radiation losses as well as the field enhancement at the triangle apex which strongly depends on its radius of curvature (i.e., a smaller tip radius of curvature results in a much higher FCF). With this definition, the calculated FCF as a function of the length L of the gold taper is plotted in Figure 3c for a moderate tip radius of curvature of 20 nm (a conservative value easily

achievable in fabrication). Moreover, in Figure 3d, the electrical field amplitude at point “Q” is computed as a monitor of light transmission in the photonic waveguide. As can be seen from a comparison of Figure 3 panels c and d, the FCF is maximum when the strength of the electric field is minimum at point “Q”. This correlation implies higher consumption of the input optical power and hence lower optical transmission. The mode-beat effect can be seen as the slow variation in each of the curves. The ripples on the curves of FCF come from weak resonances between the forward wave propagating and the reflected wave at the apex of the nanotaper (detailed analysis of these effects is available in our previous theoretical paper²⁸). A FCF of 15 is found for a length of $L = 750$ nm. It should be noted that impressive enhancement values beyond 40 are potentially achievable by reducing the tip radius to less than 5 nm, a challenge for the current nanofabrication standards yet very promising for future optimizations.

To experimentally characterize the behavior and performances of the designed PLC, we used a heterodyne apertureless near-field scanning optical microscope (NSOM).³⁷ A silicon atomic force microscope (AFM) probe with a nominal apex diameter of 15 nm was used to locally probe the optical near field. The experimental setup is equipped with polarization controllers and tapered lensed polarization-maintaining fibers to precisely control the polarization of the incident light. In order to observe the behavior of the electromagnetic modes propagating along the structure, we first removed the polarizers to excite the PLC structure with elliptical light at the wavelength of 1550 nm. The experiments were conducted for a pattern with a plasmonic nanotaper of about 750 nm. We scanned the electromagnetic modes along the structure at three different locations, in the input waveguide (Figure 4a), in the nanotaper zone (Figure 4b), and in the output waveguide (Figure 4c), respectively.

Figure 4a reveals a lightwave pattern characterized by a field highly concentrated both on the edges and on the top center of the bare waveguide. This observation indicates that both the fundamental TM-like and TE-like photonic modes propagate in the Si waveguide. As a result, the two copropagative modes induce a longitudinal periodic pattern in the near field profile that is also clearly visible. In addition, we observe very short longitudinal oscillations due to interferences between propagative and contrapropagative waves produced by reflections from the PLC and from the waveguide output facet.

The beating pattern produced by TM-like and TE-like photonic modes is also visible in the phase image (shown in the bottom row of Figure 4a, b, and c), where we note a distortion of the wavefronts and also many phase singularities at some points where the field vanishes due to destructive interferences of different modes. As expected, we observe an enhancement of the optical near field signal at the PLC location indicated by the white dashed circle in the topography image (Figure 4b, middle row). Moreover, part of the incident light also couples to radiative modes as confirmed by the presence of concentric wavefronts in the phase map in Figure 4b. An interesting observation from the amplitude and phase maps is that the interference mode beating is more pronounced in the input region and vanishes at the output region (Figure 4c). Also, it can be seen from Figure 4c that light is mostly confined at the edge of the waveguide, implying the existence of TE-like modes at the output region. This plot shows that the TM-like mode is mostly coupled to the plasmonic nanotaper and is “consumed”, whereas the TE-like mode passes through the plasmonic

nanotaper region with minimum interaction. It was expected from our theoretical analysis that the fundamental TM-like mode in the Si waveguide has a stronger coupling to the plasmonic nanotaper.

To quantify these qualitative observations, we performed a spatial Fourier analysis (1D Fast Fourier Transform) of the complex electric field along the direction of propagation to obtain the mode propagation constants. In fact, in the FFT spectra, the spatial frequencies of the peaks are directly linked to the wavenumbers of corresponding waveguide modes and, thus, to their effective indices, and the intensity of a FFT spectrum at each peak is proportional to the mode excitation power density. Therefore, this method is very powerful and enables us to measure the transmission and reflection ratios for different modes simultaneously. As shown in Figure 4d, the black curve shows the fundamental harmonics of the TM-like and TE-like modes in the input region before the plasmonic nanotaper with the effective index values of $n_{\text{TM}} = 1.83$ and $n_{\text{TE}} = 2.43$, respectively. These values agree with the simulation results of $n_{\text{TM}} = 1.6067$ and $n_{\text{TE}} = 2.3964$. The forward propagating modes are indicated by positive effective index values and the backward propagating guided modes are indicated by negative effective index values. The discrepancy between the measured and calculated effective indices is partially caused by the presence of the vertically oriented AFM silicon probe in the experiments. The difference is higher for the TM-like mode than that for the TE-like mode because of the orientation of the major component of the electric field and distribution of the modes. For the TM-like mode, the major component of the electric field is parallel to the AFM probe and its distribution overlaps strongly with the AFM probe, and thus, a strong perturbation is observed. On the other hand, for the TE mode, the major component of the electric field is perpendicular to the axis of the AFM probe and its distribution is well confined inside the Si waveguide, and therefore, a relatively small perturbation of the effective index is found. The amplitudes of the FFT spectra show the power spectral density of the modes. It is evident from the inset of Figure 4d that the power of the fundamental TM-like photonic mode (TM_0) is significantly decreased after passing through the plasmonic nanotaper due to the coupling to the plasmonic modes compared to the power of the fundamental TE-like mode. The transmittance, defined as the ratio of the output power to the input power for the TM_0 mode (inset of Figure 4d) can be obtained as $T_{\text{TM}} = 2\%$. In order to estimate the PLC intrinsic reflectance R_{TM} , we have to take into account the reflection coming from the waveguide output facet, say R_{output} . Then, from the overall reflection R_{input} measured from Figure 4a in the input waveguide, we obtain $R_{\text{TM}} = R_{\text{input}} - R_{\text{output}} = 6\%$. Therefore, the power lost by the PLC (scattering and absorption), amounts to $P_{\text{Extinction, TM}} = 92\%$. In an analogous way, the experimental transmittance and reflectance for TE-like incidence are estimated to be $T_{\text{TE}} = 32\%$ and $R_{\text{TE}} = 2\%$ respectively, leading to $P_{\text{Extinction, TE}} = 66\%$. The strong extinction of the TM incidence confirms that this mode strongly interacts with the PLC as expected from the simulations.

To go further in the experimental investigation, we fixed a TM-like incidence, and we performed a higher resolution NSOM scan over a small area on top of a plasmonic nanotaper (Figure 5). This nanotaper pattern under measurement has some shift from the central line of the waveguide. However, it barely affects the concentration efficiency as discussed in the

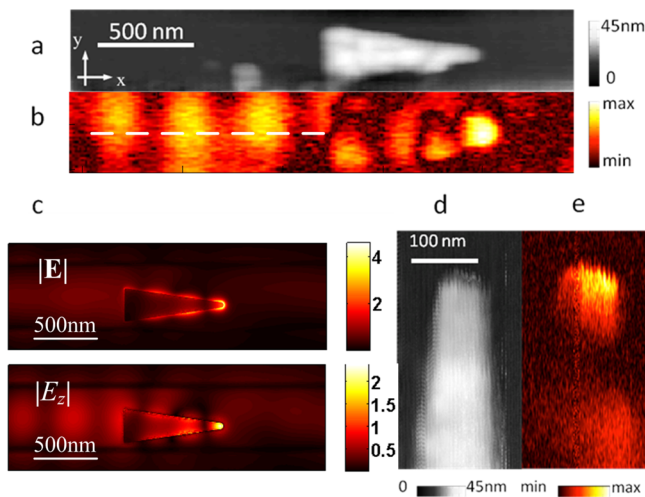


Figure 5. Measured optical near field along the integrated PLC under TM-like photonic mode excitation: (a) AFM topography and (b) optical near field amplitude around the PLC on silicon waveguide. (c) Simulated profiles ($|E|$ and $|E_z|$) of electrical field amplitude on the surface 20 nm above the geometric surface around the plasmonic pattern. (d) AFM topography and (e) high-resolution NSOM images of the PLC at the tip of the triangle.

Supporting Information. Figure 5b and e clearly demonstrates the strong nanofocusing of light at the apex of the PLC.

In addition, a standing wave pattern in a region just before the PLC can be observed as a result of the interference between the forward and backward TM-like modes originating from the reflections caused by the mismatch between the photonic waveguide mode and the hybrid modes in the PLC region. It can be seen that the amplitude profile has a strong peak at the apex. To obtain the effective mode volume of the concentrated electric field, we have measured the lateral profiles as well. The longitudinal confinement along the x -axis profile can be characterized by the full width at half-maximum of the squared electric field profile as $\Delta x_{\text{fwhm}} = 130$ nm and similarly the lateral confinement along the perpendicular direction (not shown) can be obtained as $\Delta y_{\text{fwhm}} = 100$ nm. The experimental results indicate that the effective area of the focused spot at a plane on top of the plasmonic nanotaper is thus $A_{\text{eff}} = \Delta x_{\text{fwhm}} \Delta y_{\text{fwhm}} = 0.013 \mu\text{m}^2$. This value is a direct measure of the effective mode area and is thus a confirmation of subwavelength concentration of electromagnetic radiation. The experimental effective volume ($V_{\text{eff}} = A_{\text{eff}} \Delta z$) of the electric field energy density around the apex of the nanotaper could not be measured because precise scanning of the near fields along the z -axis (Δz) is not easily possible. An estimation of the field confinement along the vertical direction, however, can be carried out using the method discussed in.³¹ The calculated effective volume is thus $V_{\text{eff,cal}} = 0.00086 \mu\text{m}^3$ (see Supporting Information), a mode volume that is 177.5 times lower than the limit of diffraction in all three dimensions ($V_{\text{eff,cal}} = 0.00563(\lambda/(2n(\mathbf{r}_{\text{max}})))^3$). Therefore, we estimate the vertical extent of the concentrated mode to be $\Delta z = 70$ nm. Here, $n(\mathbf{r}_{\text{max}})$ is the value of the index of refraction at the position maximum of the squared electric field.³⁸ Through this calculation, we calculated the effective area at several x - y planes and we found that the maximum electric field energy density is confined into the SiO_2 layer ($n(\mathbf{r}_{\text{max}}) = 1.45$). Furthermore, the calculated effective area, taken at 20 nm from the surface of the gold nanotaper, is $A_{\text{eff,cal}} = 0.0124 \mu\text{m}^2$, which agrees with the experimental value.

From our NSOM measurements, the enhancement factor (EF) at the apex of the plasmonic taper can be estimated based on the common definition of the ratio $|E_{\text{apex}}|/|E_{\text{apex},0}|$, where $|E_{\text{apex}}|$ is the electric field amplitude at the apex point with the presence of the plasmonic taper and $|E_{\text{apex},0}|$ is the electric field amplitude at the apex point without the presence of the plasmonic taper (bare waveguide) under the same input light conditions. We estimate an EF of 3.4 from our NSOM measurements (Figure 5b) as the ratio $\text{EF}^* = |E_{\text{apex}}^*|/|E_{\text{apex},0}^*|$, where $|E_{\text{apex}}^*|$ is an approximation of $|E_{\text{apex}}|$, which is measured as the maximum amplitude at the hot spot in Figure 5b and $|E_{\text{apex},0}^*|$ is an approximation of $|E_{\text{apex},0}|$ computed by averaging the field amplitude before the plasmonic taper (along the white dashed line in Figure 5b).

Although this figure of merit EF shows the power of the plasmonic taper to enhance the field amplitude, it does not show the strength of the hybrid photonic-plasmonic device to concentrate and focus the available input light power in the waveguide. The FCF, on the other hand, is a more appropriate figure of merit as it characterizes the efficiency of the device to couple the input power in the silicon waveguide to the hot spot region at the apex of the nanotaper. In order to estimate FCF from the NSOM measurements, we need to obtain the ratio $\text{FCF}^* = |E_{\text{apex}}^*|/|E_{\text{wg}}^*|$, where $|E_{\text{wg}}^*|$ is an experimental estimation of the average norm of the electric field amplitude inside the Si waveguide. Because a theoretical ratio $|E_{\text{apex},0}^{\text{th}}|/|E_{\text{wg}}^{\text{th}}|$ of ~ 1.43 can be calculated from the simulated fundamental TM-like mode profile, a measured $|E_{\text{apex},0}^*|$ leads to the experimental estimation $|E_{\text{wg}}^*| = |E_{\text{apex},0}^*|(|E_{\text{wg}}^{\text{th}}|/|E_{\text{apex},0}^{\text{th}}|) = |E_{\text{apex},0}^*|/1.43$. Using this method, we obtained the estimation FCF^* to be ~ 4.9 .

The EF and FCF computed from simulation are around 9 and 13, respectively. One main reason for the discrepancies between the experimentally obtained values for EF and FCF and the theoretical ones arises from the fact that the distance of the AFM tip from the surface of the waveguide cannot be precisely known and the field at the apex of the nanotaper rapidly change along the direction normal to the surface of the waveguide and falls off as we move away from the optimal distance. Therefore, $|E_{\text{apex}}^*|$ is quite an underestimation of $|E_{\text{apex}}|$. For comparison, Figure 5c shows the simulation results of electrical field amplitude profiles ($|E|$ and $|E_z|$) normalized to the average E-field amplitude over the cross section of the corresponding bare waveguide) 20 nm above the geometric surface of the device. Following the same way we obtain the experimental estimations EF^* and FCF^* , we perform similar computations from the simulations in Figure 5c and obtain an EF estimation of 4.4 and 5.8 from the $|E_z|$ and $|E|$ profiles, respectively, and an FCF estimation of 6.3 and 8.3 from the $|E_z|$ and $|E|$ profiles, respectively. These EF and FCF estimations are also significantly lower than their theoretical values.

The reason to also choose simulated $|E_z|$ for comparison is that the NSOM system picks out more signal of E_z component than that of the other electrical field components. The experimental results and the numerical simulations agree fairly well with an empirical assumption on the average distance of the NSOM probe from the measured surface to be around 20 nm. Moreover, the scattering differential cross section of the NSOM probe is strongly influenced by its interaction with the structure. One consequence of this interaction is that the radiation pattern detected in the far field rapidly changes depending on the position of the probe relative to the sample and to the local field polarization.³⁶ Thus, in order to quantitatively estimate the nanofocusing and enhancement

effects more precisely, measurements of the scattered field by the interaction of the probe with the nanotaper should ideally be done in all directions with a point-like probe. In our current setup, the scattered field is detected at an angle of 23 degrees from the surface of the sample, and the detection of the scattered field in our setup is limited by the numerical aperture (NA = 0.4) of the microscope objective used for light collection. Should one need to obtain more details about the nanofocusing and the enhancement effects in our hybrid structure, either a different arrangement of the NSOM setup should be used to measure the extinction in all directions or the effects of the NSOM measurements on the behavior of the device should be included in the simulations. In this Letter, our focus has been on the demonstration of the nanofocusing effect and the interplay of different modes in our proposed hybrid integrated device. Further research is needed in order to quantify the effect of the interaction between the plasmonic nanotaper and the NSOM probe particularly at its apex.

In conclusion, we experimentally demonstrated subwavelength nanofocusing of light on an integrated hybrid plasmonic–photonic light concentrator consisting of a plasmonic nanotaper vertically coupled to a silicon waveguide. A proper design of the structure results in strong coupling of light from a pure photonic TM-like mode to a trapped plasmonic mode at the apex of the nanotaper. It was experimentally demonstrated that in such hybrid structures, if carefully designed, the interplay between adiabatic transition, mode beating, and local resonance effects result in an extremely high-intensity focused spot at the apex. Moreover almost 92% of the input power can be converted to scattering and absorption by the plasmonic nanotaper. The Fourier analysis of the electromagnetic fields in near field verifies theoretical predictions that only TM-like modes in the waveguide can couple to the trapped plasmonic mode. This provides opportunities for multiplexing different functionalities (e.g., trapping and sensing) by using different polarizations in the same structure. The optical near field measurements revealed the high electric field concentration at the apex of the nanotaper. The measured effective area of the focus spot at the apex of the nanotaper was $0.013 \mu\text{m}^2$, with an estimated effective mode volume of $0.00563(\lambda/(2n(r_{\text{max}})))^3$. A field concentration factor (FCF) of about 4.9 is estimated from our NSOM measurements for a sample device with a radius of curvature of about 20 nm at the apex of the nanotaper.

■ ASSOCIATED CONTENT

📄 Supporting Information

Video of time-domain simulation of on-chip nanofocusing, fabrication description, simulation fabrication imperfection, eigenmode analysis of the hybrid photonic–plasmonic structure, and effective mode volume calculations. This material is available free of charge via the Internet at <http://pubs.acs.org>.

■ AUTHOR INFORMATION

Corresponding Authors

*E-mail: sylvain.blaize@utt.fr.

*E-mail: adibi@ece.gatech.edu.

Present Addresses

[¶]Université de technologie de Troyes, 12 Rue Marie Curie CS 42060, 10004 Troyes, France.

[§]Georgia Institute of Technology, 777 Atlantic Drive NW, Atlanta, Georgia 30318, United States.

^{||}Department of Mathematics, Rice University.

[‡]Department of Electrical Engineering and Computer Science, University of California Berkeley.

Notes

The authors declare no competing financial interest.

■ ACKNOWLEDGMENTS

The authors thank Qing Li for his help in the fabrication process. The work at Georgia Institute of Technology was supported by the Defense Advanced Research Projects Agency (DARPA) under Contract HR 0011-10-1-0075 through the DARPA CIPHER Project (S. Rodgers). The French authors thank the RCA (Région Champagne-Ardenne, France, contract PLASMOBIO) and the Labex ACTION project (French research agency contract ANR-11-LABX-01-01) for financial support.

■ REFERENCES

- (1) Kohoutek, J.; Dey, D.; Bonakdar, A.; Gelfand, R.; Sklar, A.; Memis, O. G.; Mohseni, H. *Nano Lett.* **2011**, *11*, 3378–3382.
- (2) Wang, K.; Schonbrun, E.; Steinvurzel, P.; Crozier, K. B. *Nano Lett.* **2010**, *10*, 3506–3511.
- (3) Reece, P. J. *Nat. Photonics* **2008**, *2*, 333–335.
- (4) Coppens, Z. J.; Li, W.; Walker, D. G.; Valentine, J. G. *Nano Lett.* **2013**, *13*, 1023–1028.
- (5) Gao, H.; Yang, J.-C.; Lin, J. Y.; Stuparu, A. D.; Lee, M. H.; Mirsich, M.; Odom, T. W. *Nano Lett.* **2010**, *10*, 2549–2554.
- (6) Alavirad, M.; Roy, L.; Berini, P. *IEEE J. Sel. Top. Quantum Electron.* **2014**, *20*, 1–8.
- (7) Hentschel, M.; Utikal, T.; Giessen, H.; Lippitz, M. *Nano Lett.* **2012**, *12*, 3778–3782.
- (8) Kinkhabwala, A.; Yu, Z.; Fan, S.; Avlasevich, Y.; Müllen, K.; Moerner, W. *Nat. Photonics* **2009**, *3*, 654–657.
- (9) Novotny, L.; Bian, R. X.; Xie, X. S. *Phys. Rev. Lett.* **1997**, *79*, 645–648.
- (10) Ropers, C.; Neacsu, C.; Elsaesser, T.; Albrecht, M.; Raschke, M.; Lienau, C. *Nano Lett.* **2007**, *7*, 2784–2788.
- (11) Nerkararyan, K. V. *Phys. Lett. A* **1997**, *237*, 103–105.
- (12) Vernon, K. C.; Gramotnev, D. K.; Pile, D. F. *J. Appl. Phys.* **2007**, *101*, 104312–104312.
- (13) Verhagen, E.; Kuipers, L.; Polman, A. *Nano Lett.* **2010**, *10*, 3665–3669.
- (14) Babadjanyan, A.; Margaryan, N.; Nerkararyan, K. V. *J. Appl. Phys.* **2000**, *87*, 3785–3788.
- (15) Stockman, M. I. *Phys. Rev. Lett.* **2004**, *93*, 137404–137404.
- (16) Gramotnev, D. K. *J. Appl. Phys.* **2005**, *98*, 104302–104302.
- (17) Pile, D.; Gramotnev, D. K. *Appl. Phys. Lett.* **2006**, *89*, 041111–041111.
- (18) Issa, N. A.; Guckenberger, R. *Plasmonics* **2007**, *2*, 31–37.
- (19) Verhagen, E.; Polman, A.; Kuipers, L. K. *Opt. Express* **2008**, *16*, 45–57.
- (20) Volkov, V. S.; Bozhevolnyi, S. I.; Rodrigo, S. G.; Martin-Moreno, L.; Garcia-Vidal, F. J.; Devaux, E.; Ebbesen, T. W. *Nano Lett.* **2009**, *9*, 1278–1282.
- (21) Choi, H.; Pile, D. F.; Nam, S.; Bartal, G.; Zhang, X. *Opt. Express* **2009**, *17*, 7519–7524.
- (22) Vedantam, S.; Lee, H.; Tang, J.; Conway, J.; Staffaroni, M.; Yablonovitch, E. *Nano Lett.* **2009**, *9*, 3447–3452.
- (23) Lindquist, N. C.; Naggal, P.; Lesuffleur, A.; Norris, D. J.; Oh, S.-H. *Nano Lett.* **2010**, *10*, 1369–1373.
- (24) Choo, H.; Kim, M.-K.; Staffaroni, M.; Seok, T. J.; Bokor, J.; Cabrini, S.; Schuck, P. J.; Wu, M. C.; Yablonovitch, E. *Nat. Photonics* **2012**, *6*, 838–844.
- (25) Lafone, L.; Sidiropoulos, T. P.; Oulton, R. F. *Opt. Lett.* **2014**, *39*, 4356–4359.
- (26) He, X.; Yang, L.; Yang, T. *Opt. Express* **2011**, *19*, 12865–12872.

- (27) Desiatov, B.; Goykhman, I.; Levy, U. *Opt. Express* **2011**, *19*, 13150–13157.
- (28) Luo, Y.; Chamanzar, M.; Adibi, A. *Opt. Express* **2013**, *21*, 1898–1910.
- (29) Dionne, J. A.; Sweatlock, L. A.; Sheldon, M. T.; Alivisatos, A.; Atwater, H. A. *IEEE J. Sel. Top. Quantum.* **2010**, *16*, 295–306.
- (30) Delacour, C.; Blaize, S.; Grosse, P.; Fedeli, J. M.; Bruyant, A.; Salas-Montiel, R.; Lerondel, G.; Chelnokov, A. *Nano Lett.* **2010**, *10*, 2922–2926.
- (31) Salas-Montiel, R.; Apuzzo, A.; Delacour, C.; Sedaghat, Z.; Bruyant, A.; Grosse, P.; Chelnokov, A.; Lerondel, G.; Blaize, S. *Appl. Phys. Lett.* **2012**, *100*, 231109–231109.
- (32) Février, M.; Gogol, P.; Aassime, A.; Mégy, R.; Delacour, C.; Chelnokov, A.; Apuzzo, A.; Blaize, S.; Lourtioz, J.-M.; Dagens, B. *Nano Lett.* **2012**, *12*, 1032–1037.
- (33) Bernal Arango, F.; Kwadrin, A.; Koenderink, A. F. *ACS Nano* **2012**, *6*, 10156–10167.
- (34) Chamanzar, M.; Xia, Z.; Yegnanarayanan, S.; Adibi, A. *Opt. Express* **2013**, *21*, 32086–32098.
- (35) Gramotnev, D. K.; Bozhevolnyi, S. I. *Nat. Photonics* **2014**, *8*, 13–22.
- (36) Apuzzo, A.; Février, M.; Salas-Montiel, R.; Bruyant, A.; Chelnokov, A.; Léron del, G.; Dagens, B.; Blaize, S. *Nano Lett.* **2013**, *13*, 1000–1006.
- (37) Stefanon, I.; Blaize, S.; Bruyant, A.; Aubert, S.; Lerondel, G.; Bachelot, R.; Royer, P. *Opt. Express* **2005**, *13*, 5553–5564.
- (38) Robinson, J. T.; Manolatos, C.; Chen, L.; Lipson, M. *Phys. Rev. Lett.* **2005**, *95*, 143901.